Nanoscale

PAPER

View Article Online
View Journal | View Issue

Cite this: *Nanoscale*, 2019, **11**, 109

Direct Z scheme-fashioned photoanode systems consisting of Fe_2O_3 nanorod arrays and underlying thin Sb_2Se_3 layers toward enhanced photoelectrochemical water splitting performance†

Aizhen Liao,[a,b] Yong Zhou, *[a,b,c] Leixin Xiao,[d] Chunfeng Zhang,[b] Congping Wu,[a,b,c] Adullah M. Asiri,[e] Min Xiao[b] and Zhigang Zou[a,b,d,c]

Received 13th October 2018,
Accepted 2nd December 2018

DOI: 10.1039/c8nr08292h

rsc.li/nanoscale

An elegant Z-scheme-fashioned photoanode consisting of Fe_2O_3 nanorod arrays and underlying thin Sb_2Se_3 layers was rationally constructed. The photocurrent density of the Sb_2Se_3–Fe_2O_3 Z-scheme photoanode reached 3.07 mA cm^{-2} at 1.23 V *vs.* RHE, three times higher than that of pristine Fe_2O_3 at 1.03 mA cm^{-2}. An obvious cathodic shift of the photocurrent onset potential of about 200 mV was also observed. The transient photovoltage response demonstrates that the suitable band edges (E_{CB} ~ −0.4 eV and E_{VB} ~ 0.8 eV) of Sb_2Se_3, match well with Fe_2O_3 (E_{CB} ~ 0.29 eV and E_{VB} ~ 2.65 eV), permitting the photoexcited electrons on the conduction band of the Fe_2O_3 to transfer to the valence band of Sb_2Se_3, and recombine with the holes therein, thus allowing a high concentration of holes to collect in the Fe_2O_3 for water oxidation. The transient absorption spectra further corroborate that the built-in electric field in the p–n heterojunction leads to a more effective separation and a longer lifetime of the charge carriers.

Introduction

Solar water splitting in photoelectrochemical (PEC) cells has drawn much attention for sustainable hydrogen production, owing to the limited reserve of fossil fuels and the increasing concern of environmental pollution.[1–3] Photoanodes for water oxidation are the rate-limiting step for the PEC overall water splitting efficiency. Hematite (α-Fe_2O_3), an n-type semiconductor with a suitable narrow band gap (2.2 eV), has emerged as one of the most attractive photoanode candidates because of its low cost, (photo)-electrochemical stability, non-toxicity, and earth-abundance.[4–7] However, α-Fe_2O_3 suffers from sluggish water oxidation kinetics, severe surface recombination, poor lifetimes of carriers, and short hole migration distance.[8–10] Great efforts such as surface passivation, nanostructure engineering, selective doping, and oxygen evolution cocatalysts have been made to improve its PEC performance.[11–15] However, the α-Fe_2O_3 photoanode developed so far still shows a lower photocurrent density relative to its theoretical maximum of 12.6 mA cm^{-2} at 1.23 V *versus* the reversible hydrogen electrode (*vs.* RHE) under AM 1.5G illumination (100 mW cm^{-2}).[9,16] Obviously, a single Fe_2O_3 component cannot satisfy the requirement of efficiently steering the spatial separation/transfer of electron–hole pairs for high PEC performance. The conjugation of coupling with other semiconductors has been proven an efficient method for solving the weaknesses above by providing a built-in electric field and optimal transportation path.[17] Type II heterostructures have been commonly built, allowing photogenerated electrons (holes) to be transferred from one semiconductor with a higher conduction (lower valence) band (CB) to that with a lower conduction (higher valence) band (VB).[18] However, the redox ability of this type of heterojunction is dynamically lowered after charge flowing, compared to individual components.

Z-scheme photocatalyst systems by mimicking natural photosynthesis in green plants are designed to employ two semiconductors with one H_2 production photocatalyst and one O_2 production photocatalyst.[19] The Z-scheme semiconductor heterojunction possesses a vectorial charge transfer feature,

[a]*Eco-Materials and Renewable Energy Research Center (ERERC), Jiangsu Key Laboratory for Nano Technology, Nanjing University, Nanjing 210093, China. E-mail: zhouyong1999@nju.edu.cn*
[b]*National Laboratory of Solid State Microstructures, Collaborative Innovation Center of Advanced Microstructures, School of Physics, Nanjing University, Nanjing 210093, P. R. China*
[c]*Sunlite Ltc, Kunshan Innovation Institute of Nanjing University, Kunshan, Jiangsu 215347, P. R. China*
[d]*School of Engineering and Applied Science, Nanjing University, Nanjing 210093, P. R. China*
[e]*King Abdulaziz University, Chemistry Department, Faculty of Science, Jeddah 21589, Saudi Arabia*
†Electronic supplementary information (ESI) available. See DOI: 10.1039/c8nr08292h

i.e. the photo-induced electrons on the semiconductor with a lower conduction band (CB) potential will combine with the holes on another semiconductor with a higher valence band (VB) potential, and leave the electrons and holes in reduction-evolving and oxidation-evolving semiconductors, respectively. It simultaneously leads to superior charge separation and perseveration of the strong redox ability of each component.[18] A direct Z-scheme free of electron mediators provides energetically favorable band alignment for facile migration of charge across the interface in the heterojunction region. While many α-Fe_2O_3-based Z-schemes of powder systems have been established, such as with g-C_3N_4,[20–22] scarcely have well-constructed Fe_2O_3 Z-scheme photoanodes been used for the PEC reaction, especially Fe_2O_3 nanorod array-based ones, which are beneficial for direct charge transfer to conductive substrates.

Sb_2Se_3 is a direct band gap (1.0–1.3 eV), low-cost, and p-type semiconductor composed of non-toxic and earth-abundant elements, which possesses wide applications in solar selective and decorative coatings, as well as optical and thermoelectric cooling devices.[23,24] Sb_2Se_3 possesses a high absorption coefficient of 10^5 cm^{-1} in the visible range and has been selected as a promising photocathode for water splitting into H_2.[20,25,26]

In this work, a direct Z-scheme-fashioned photoanode consisting of Fe_2O_3 nanorod arrays and underlying thin Sb_2Se_3 layers free of electron mediators was for the first time rationally constructed. The photocurrent density of the elegant Sb_2Se_3–Fe_2O_3 Z-scheme photoanode reaches 3.07 mA cm^{-2} at 1.23 V *vs.* RHE, three times higher than that of pristine Fe_2O_3 at 1.03 mA cm^{-2}. An obvious cathodic shift of the photocurrent onset potential of about 200 mV is also observed. The transient photovoltage (TPV) response demonstrates that the photoexcited electrons on the CB of the Fe_2O_3 transfer to the VB of Sb_2Se_3, and recombine with the holes therein, allowing a high concentration of the holes to be collected in the Fe_2O_3 for water oxidation. The transient absorption (TA) spectra corroborate that the built-in electric field in the p–n heterojunction leads to a more effective separation and longer lifetimes of the charge carriers. The selection of Sb_2Se_3 for the construction of the present Z-scheme photoanode system has several advantages: (1) the band edges ($E_{CB} \sim -0.4$ eV and $E_{VB} \sim 0.8$ eV) of Sb_2Se_3 match well with Fe_2O_3 ($E_{CB} \sim 0.29$ eV and $E_{VB} \sim 2.65$ eV) for the Z-scheme; (2) Sb_2Se_3 is a promising light-absorbing material with the property of efficient charge separation; (3) the narrow bandgap allows the material to absorb as much as possible near-infrared light, extending the range of the light absorption; (4) Sb_2Se_3 possesses a much higher hole mobility up to 42 cm^2 V^{-1} s^{-1} compared to 0.2 cm^2 V^{-1} s^{-1} of Fe_2O_3. It allows the holes of Sb_2Se_3 to move fast and arrive on the interface of the Sb_2Se_3/Fe_2O_3 prior to those of Fe_2O_3 recombining with the electrons of the Fe_2O_3, thus reducing the intrinsic charge recombination of Fe_2O_3; (5) Sb_2Se_3 shows an Ohmic junction with the underlying FTO with a small interface resistance, which allows the electrons from the Sb_2Se_3/Fe_2O_3 to smoothly flow to the FTO substrate, in contrast to the high resistance of the pristine Fe_2O_3 with FTO due to the Schottky junction.

Experimental section

Preparation of the Fe_2O_3/Sb_2Se_3 photoanode

The fabrication of the Sb_2Se_3/Fe_2O_3 Z-scheme photoanode starts with the deposition of a thin Sb_2Se_3 layer on a fluorine-doped tin oxide (FTO) substrate through thermal evaporation. The evaporator source is commercially available Sb_2Se_3 powder (antimony(III) selenide, AR, 99.9%). The details of the process are as follows, the FTO glass (1 cm × 2 cm) was cleaned with deionized (DI) water, acetone, and ethanol, and then was placed a few cm apart from the Sb_2Se_3 powder, inside a quartz tube. With ~200 sccm of high-purity Ar gas, the furnace temperature was raised to 550 °C. After 30 min of deposition, the furnace was allowed to cool to room temperature under the argon flow, resulting in a successfully uniform coating of Sb_2Se_3 on the FTO substrate. FeOOH nanorods were then vertically aligned on the Sb_2Se_3 nanosheets according to the reported methods by our group. More details were described previously.[27] Finally, the Sb_2Se_3/FeOOH was heated at 550 °C for 120 minutes in Ar atmosphere, and subsequently at 650 °C for 15 min resulting in the formation of Sb_2Se_3/Fe_2O_3. As a comparison, the Fe_2O_3 nanorods were synthesized under the same growth conditions, except for the step of deposition of a thin Sb_2Se_3 layer on a FTO substrate through thermal evaporation.

Sample characterization

A FEI NOVA NanoSEM230 scanning electron microscope is employed to investigate the morphology of the samples. The crystal structure of the samples is identified by X-ray diffraction (XRD) (Ultima III, Rigaku) with Cu Kα radiation (k = 0.154 nm). Transmission electron microscope (TEM) images are taken on a JEM 200CX TEM apparatus. X-ray photoelectron spectroscopy (XPS) is carried out on a Thermo Scientific K-Alpha instrument operating with an unmonochromatized Al Kα X-ray source, and the data are calibrated by the binding energy of the C 1s line at 283.6 eV. A Shimadzu UV-2550 spectrometer equipped with an integrating sphere is used to investigate the absorption properties of the samples. Electrochemical impedance spectroscopic (EIS) curves are measured by a PAR2273 workstation (Princeton Applied Research, USA) under a forward bias of 0.2 V and AM 1.5G illumination. Transient photovoltage (TPV) based on the lock-in amplifier measurement were carried out on a home-made system of Tengfeng Xie's group of Jilin University, which researches the separation and kinetic behaviors of photogenerated charge carriers.[28,29] The TPV measurement was performed under the illumination of a 355 nm laser pulse.

Photoelectrochemical property measurements

The photoelectrochemical (PEC) performance of the photoanodes is investigated in a three-electrode cell using an electrochemical analyzer (CHI-630D, Shanghai Chenhua) under AM 1.5G illumination. The electrolyte is a 1 M NaOH aqueous solution (pH 13.6). The Fe_2O_3 sample is used as the working electrode. A Pt foil and a saturated Ag/AgCl electrode are used

as the counter and reference electrode. The RHE potential is calculated following the formula $V_{RHE} = V_{Ag/AgCl} + 0.059\ pH + E_{Ag/AgCl}$, where V_{RHE} is the converted potential *versus* RHE, and $E^{\circ}_{Ag/AgCl} = 0.1976$ V at 25 °C. The active area of the Fe_2O_3 sample is fixed to 0.28 cm^2 using a black mask. A cyclic voltammetry method is adopted with a scan rate of 10 mV s^{-1}.

Results and discussion

The fabrication of the Sb_2Se_3/Fe_2O_3 Z-scheme photoanode starts with the deposition of a thin Sb_2Se_3 layer on a fluorine-doped tin oxide (FTO) substrate through thermal evaporation (Scheme 1). The FeOOH nanorod array was then hydrothermally grown onto the surface of the Sb_2Se_3/FTO, and subsequently annealed in an inert atmosphere to transfer into Fe_2O_3. The FE-SEM image from the top view of the FTO/Sb_2Se_3 film clearly shows the apparent difference of the surface of the FTO substrate before (Fig. 1a) and after (Fig. 1b and Fig. S1a†) deposition of the Sb_2Se_3. The formed Sb_2Se_3 layer consists of nanosheet-like particles with full coverage of the FTO substrate. FE-SEM elemental mapping and the EDX spectrum demonstrate the presence of Sb and Se elements (Fig. S2†). The corresponding cross-sectional FE-SEM image reveals the thickness of the Sb_2Se_3 layer to be approximately 120 nm (Fig. 1c). Fig. 1d and e show the cross-section and top view of the vertical growth of the Fe_2O_3 nanorods on the surface of the Sb_2Se_3 layer, respectively. No morphological differences of the Fe_2O_3 nanorod array were observed between the Sb_2Se_3/FTO and the FTO (Fig. S1b and S1c†), which indicates that the presence of the Sb_2Se_3 layer has no effect on the rod-like crystal growth of Fe_2O_3. Fig. S3† shows the UV-Vis absorption spectra of Sb_2Se_3, Fe_2O_3, and the Sb_2Se_3/Fe_2O_3 film.

The XRD patterns clearly show the characteristic diffraction peaks of hematite (Fe_2O_3; JCPDS 79-0007) and FTO (Fig. S4†). No Sb_2Se_3 diffraction peaks are identified in the composite film, possibly due to the thinness of the Sb_2Se_3. The high-resolution XPS profiles of the Sb_2Se_3 film display the peak positions at binding energies of 530.1 and 538.5 eV, corresponding to Sb $3d_{5/2}$ and Sb $3d_{3/2}$, respectively (Fig. 2a). The Se 3d spectrum exhibits two peaks of Se $3d_{5/2}$ and Se $3d_{3/2}$ (Fig. 2b), consistent with Se^{2-} in the case of Sb_2Se_3.[30,31] The Fe 2p high-resolution XPS of both Fe_2O_3 and the Sb_2Se_3/Fe_2O_3 films can be fitted into Fe $2p_{1/2}$ and Fe $2p_{3/2}$ peaks, centered at binding energies of 723.5 eV and 711.4 eV, respectively, typical values for Fe^{3+} in Fe_2O_3.[32,33] Satellite peaks at 717.2 eV indexible to Fe^{2+} were observed in both pristine Fe_2O_3 and Sb_2Se_3/Fe_2O_3, originating from the annealing process-inducing oxygen vacancy (Fig. 2c).[34] The O 1s peak can be assigned to two main constituent peaks at 528.9 and 530.4 eV, corresponding to the Fe–O band and OH^-, respectively (Fig. 2d).

The PEC performance of the Sb_2Se_3/Fe_2O_3 photoanode is dependent on the film thickness of the Sb_2Se_3 layer (Fig. S5†). 15 min deposition cannot obtain an observable film due to its too thin thickness (Fig. S5b†). It may result in a non-consecutive Sb_2Se_3 layer, incompletely covering the FTO substrate, and subsequently leading to the reverse reaction, decreasing the PEC performance. 60 and 90 min deposition generates ~300 nm and ~500 nm thick Sb_2Se_3 films (Fig. S5d and S5e†), in which the holes need to move down a long pathway to recombine with the electrons of Fe_2O_3, also depressing the

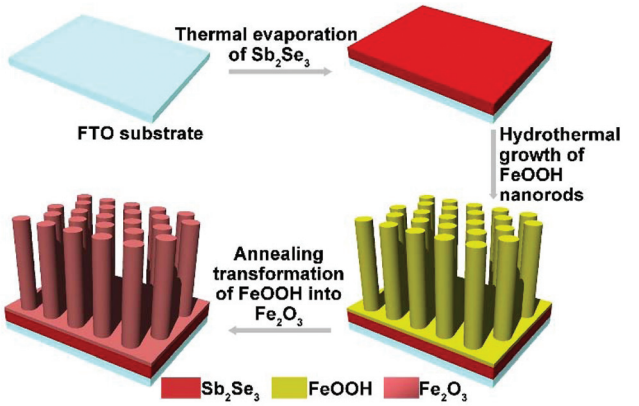

Scheme 1 Schematic illustration of the fabrication process of Sb_2Se_3/Fe_2O_3.

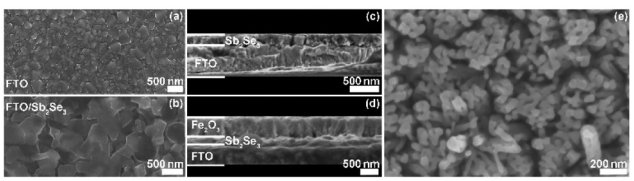

Fig. 1 (a) FE-SEM image of FTO. (b and c) Top- and cross-sectional view FE-SEM images of Sb_2Se_3 with 30 min deposition on the FTO substrate, respectively. (d and e) Cross-sectional and top-view SEM images of Sb_2Se_3/Fe_2O_3, respectively.

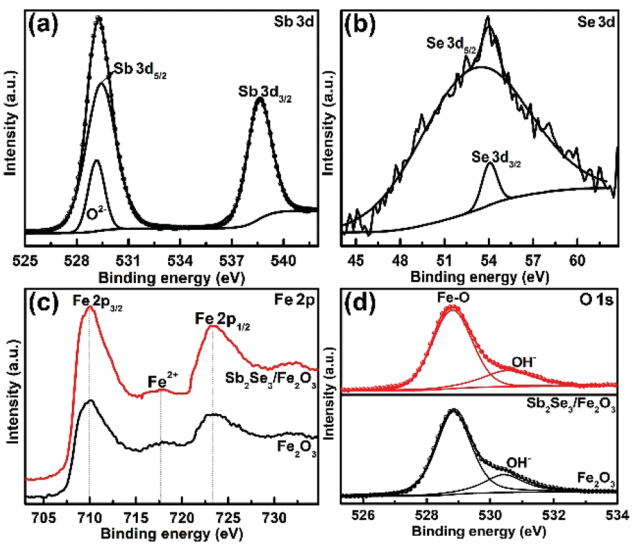

Fig. 2 High-resolution XPS (a) Sb 3d, (b) Se 3d signal peak of Sb_2Se_3, (c) Fe 2p, and (d) O 1s spectra of Fe_2O_3 and Sb_2Se_3/Fe_2O_3.

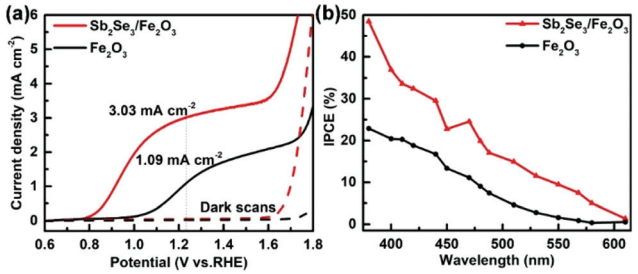

Fig. 3 (a) Photocurrent–potential (J–V) curves of the Fe_2O_3 and Sb_2Se_3/Fe_2O_3 photoanodes with 30 min deposition of the Sb_2Se_3 layer under 1 M NaOH (pH ~ 13.6) aqueous electrolyte under AM 1.5G illumination and in the dark and (b) corresponding IPCE plots obtained and collected at 1.23 V *vs.* RHE.

PEC performance. The Sb_2Se_3/Fe_2O_3 with 30 min deposition of about 120 nm thickness exhibits a maximum photocurrent density of 3.03 mA cm^{-2} at 1.23 V *vs.* RHE, about three times higher than pristine Fe_2O_3 (1.09 mA cm^{-2} at 1.23 V *vs.* RHE) (Fig. S5c† and Fig. 3a). The corresponding onset potential also obviously cathodically-shifts about 200 mV from 1.00 to 0.80 V. In addition, the Sb_2Se_3/Fe_2O_3 photoanode displays a significantly enhanced incident photon-to-current conversion efficiency (IPCE) of 48.5% at 380 nm, double that of pristine Fe_2O_3 at 22.9% (Fig. 3b). While the Sb_2Se_3 film alone is a p-type semiconductor which behaves as an insulator under positive bias, the increase of the PEC performance can be ascribed to the unique charge separation mechanism of the Z-scheme system. Furthermore, the Sb_2Se_3/Fe_2O_3 photoanode exhibits considerable stability, and the photocurrent only decreased by 12% after 5.6 h of continuous illumination (Fig. S6†).

The TPV responses for the Sb_2Se_3/Fe_2O_3 and Fe_2O_3 with 355 nm laser illumination were detected with a logarithmical time scale through light illumination from top to bottom electrodes (Fig. 4). The TPV spectra of both photoanodes reveal a positive sign response, implying that the holes move toward and accumulate on the top electrode,[34–36] *i.e.* the Fe_2O_3 side. The Sb_2Se_3/Fe_2O_3 displays an almost three-times stronger intensity of TPV signal than the pristine Fe_2O_3, which can be ascribed to the strong charge carrier separation ability of this structure and high concentration of holes collected in the Fe_2O_3 with a long surviving time. The Z-scheme mode of the Sb_2Se_3/Fe_2O_3 can be schematically illustrated (Fig. 4b). Under light illumination, both Sb_2Se_3 and Fe_2O_3 are photoexcited to generate electron–hole pairs. The electrons in the CB of the Fe_2O_3 shift to the VB of the Sb_2Se_3 and recombine with the holes therein. The depletion of the electrons of Fe_2O_3 restrains the intrinsic charge recombination of the Fe_2O_3, allowing the longer survival time of the holes, which are highly oxidative, and can readily perform oxygen evolution reactions at the electrode/electrolyte interface. Meanwhile, the concentrated electrons in the Sb_2Se_3 side are highly reductive, which then transfer to the counter electrode to efficiently drive hydrogen production.

To explore the impact of Sb_2Se_3 on the photogenerated charge carrier dynamics, the TA spectra of the pristine Fe_2O_3 and Sb_2Se_3/Fe_2O_3 on a 0–6393 ps time scale were probed after 350 nm laser excitation (Fig. 5a and b). Across the probed wavelength range, both the films display two excited state absorption (ESA) signal peaks, a weak one at ~500 nm and a strong one at ~575 nm. Two peaks showing a similar time-decay tendency derive from the absorption of photo-generated holes with different energy levels.[37] The ESA signal at the latter was the main spectroscopic feature in the hematite sample, which can be attributed to the absorption of photo-generated holes.[38–40] The TA spectrum of Sb_2Se_3/Fe_2O_3 exhibits a higher intensity and a slow time-dependent decay rate within the monitored time range, compared with the Fe_2O_3. It suggests that the Sb_2Se_3/Fe_2O_3 possesses more photogenerated holes and a lower recombination rate of carriers, further confirming the Z-scheme structure. The time profiles of the TA probed at 575 nm were fitted by a two-exponential function in Fig. 5c. The Sb_2Se_3/Fe_2O_3 shows a relatively slower decay than the Fe_2O_3 in the 9–18 ps windows, and the lifetimes for the Fe_2O_3 and Sb_2Se_3/Fe_2O_3 were detected 2.1 ps and 3.7 ps, respectively, indicating that the Z-scheme heterostructure is beneficial for separation of the photogenerated charges, and maintaining the separation long enough for the surface reaction of water oxidation. The open-circuit photovoltage (OCPV) calculated from the difference of the open-circuit potentials between dark and illumination reveals that the OCPV values of Sb_2Se_3/Fe_2O_3 was higher in comparison with the pristine Fe_2O_3, additionally demonstrating the improvement of the charge separation efficiency (Fig. S7†).

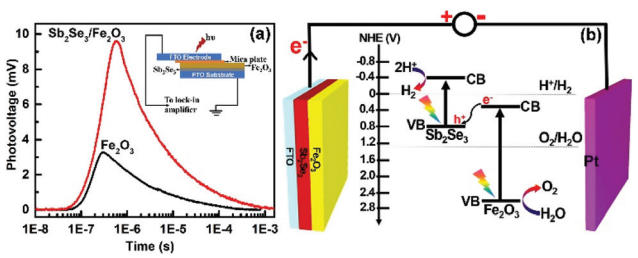

Fig. 4 (a) TPV of Fe_2O_3 and Sb_2Se_3/Fe_2O_3. The wavelength and intensity of the excitation pulse are 355 nm and 100 μJ, respectively. Inset: Schematic setup of the TPV measurement. (b) Schematic illustration of the charge transfer on the Sb_2Se_3/Fe_2O_3 photoanode.

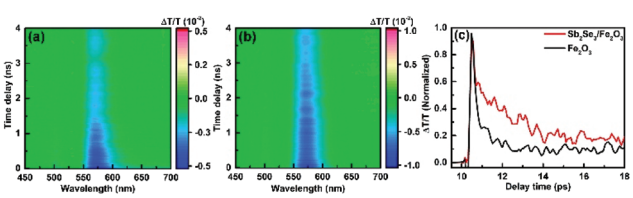

Fig. 5 Two-dimensional color maps of the obtained transient absorption data for (a) Fe_2O_3 and (b) Sb_2Se_3/Fe_2O_3. (c) Normalized transient absorption *vs.* time curves of Fe_2O_3 and Sb_2Se_3/Fe_2O_3 in air atmosphere, λ_{ex} = 350 nm, at 575 nm.

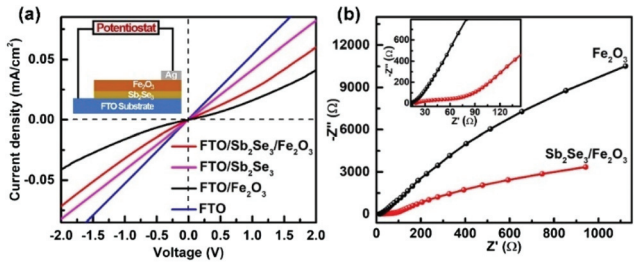

Fig. 6 (a) Solid-state *J–V* characteristics of FTO, FTO/Fe_2O_3 and FTO/Sb_2Se_3/Fe_2O_3. (b) The EIS under AM 1.5G simulated sunlight illumination.

Solid-state current–voltage (*J–V*) characterization was conducted. FTO and Ag were used as the front and back contacts, respectively. While the pristine Fe_2O_3 film displays rectifying characteristics to form a Schottky junction with FTO, the linear *J–V* feature of the FTO/Sb_2Se_3 indicates an Ohmic junction formation of the Sb_2Se_3 with FTO. The steep slope close to that of the FTO implies a small contact resistance at the interface of the Sb_2Se_3/FTO, which allows the electrons from the Sb_2Se_3 to smoothly flow to the FTO substrate. The increased slope of the Sb_2Se_3/Fe_2O_3 compared with pristine Fe_2O_3 clearly states that more electrons in the former transfer to the FTO substrate in comparison with the latter. The electrochemical impedance spectroscopy (EIS) semicircle for the Sb_2Se_3/Fe_2O_3 photoanode displays a smaller diameter than Fe_2O_3, also demonstrating that the interface charge transfer rate increases after combination of the thin Sb_2Se_3 layer (Fig. 6b).

Conclusion

A novel direct Sb_2Se_3/Fe_2O_3 Z-scheme system was successfully constructed through a vapor deposition process of a thin layer of Sb_2Se_3 on a FTO substrate, followed by growth of Fe_2O_3. The elegant Z-scheme Sb_2Se_3/Fe_2O_3 reaches a photocurrent density of 3.03 mA cm^{-2} at 1.23 V *vs.* RHE, and shows an extraordinary cathodic shift of the onset potential of about 200 mV. The enhanced PEC performance is ascribed to the unique charge separation and transfer mechanism. This study may not only inspire further development of new direct solid-state Z-scheme systems for solar water splitting with superior performance, but also could be significant in meeting the demands of environmental domains.

Conflicts of interest

There are no conflicts to declare.

Acknowledgements

This work was supported by 973 Programs (No. 2014CB239302), NSF of China (No. 21773114 and 21473091), NSF of Jiangsu Province (No. BK20171246). Additionally, the TPV measurement was greatly supported by Prof. Tengfeng Xie of Jilin University, China.

Notes and references

1 M. Gratzel, *Nature*, 2001, **414**, 338–344.
2 M. G. Walter, E. L. Warren, J. R. McKone, S. W. Boettcher, Q. Mi, E. A. Santori and N. S. Lewis, *Chem. Rev.*, 2010, **110**, 6446–6473.
3 H. Wang, H. W. Lee, Y. Deng, Z. Lu, P. C. Hsu, Y. Liu, D. Lin and Y. Cui, *Nat. Commun.*, 2015, **6**, 7261–7269.
4 A. Fujishima and K. Honda, *Nature*, 1972, **238**, 37–38.
5 H. G. Cha, S. J. Kim, K. J. Lee, M. H. Jung and Y. S. Kang, *J. Phys. Chem. C*, 2011, **115**, 19129–19135.
6 J. Y. Zheng, M. J. Kang, G. Song, S. I. Son, S. P. Suh, C. W. Kim and Y. S. Kang, *CrystEngComm*, 2012, **14**, 6957–6961.
7 H. G. Cha, M. J. Kang, I. C. Hwang, H. Kim, K. B. Yoon and Y. S. Kang, *Chem. Commun.*, 2015, **51**, 6407–6410.
8 G. Wang, Y. Ling, D. A. Wheeler, K. E. George, K. Horsley, C. Heske, J. Z. Zhang and Y. Li, *Nano Lett.*, 2011, **11**, 3503–3509.
9 H. G. Cha, J. Song, H. S. Kim, W. Shin, K. B. Yoon and Y. S. Kang, *Chem. Commun.*, 2011, **47**, 2441–2443.
10 T. K. Van, H. G. Cha, C. K. Nguyen, S. W. Kim, M. H. Jung and Y. S. Kang, *Cryst. Growth Des.*, 2012, **12**, 862–868.
11 Y. Kuang, Q. Jia, H. Nishiyama, T. Yamada, A. Kudo and K. Domen, *Adv. Energy Mater.*, 2016, **6**, 1501645–1501652.
12 G. Liu, J. Shi, F. Zhang, Z. Chen, J. Han, C. Ding, S. Chen, Z. Wang, H. Han and C. Li, *Angew. Chem., Int. Ed.*, 2014, **53**, 7295–7299.
13 G. Liu, S. Ye, P. Yan, F. Xiong, P. Fu, Z. Wang, Z. Chen, J. Shi and C. Li, *Energy Environ. Sci.*, 2016, **9**, 1327–1334.
14 Z. Lin, J. Li, Z. Zheng, L. Li, L. Yu, C. Wang and G. Yang, *Adv. Energy Mater.*, 2016, **6**, 1600510–1600520.
15 F. Le Formal, E. Pastor, S. D. Tilley, C. A. Mesa, S. R. Pendlebury, M. Grätzel and J. R. Durrant, *J. Am. Chem. Soc.*, 2015, **137**, 6629–6637.
16 J. Y. Kim, D. H. Youn, K. Kang and J. S. Lee, *Angew. Chem., Int. Ed.*, 2016, **55**, 10854–10858.
17 J. Schneider, M. Matsuoka, M. Takeuchi, J. Zhang, Y. Horiuchi, M. Anpo and D. W. Bahnemann, *Chem. Rev.*, 2014, **114**, 9919–9986.
18 H. Li, Y. Zhou, W. Tu, J. Ye, Y. Zhou and Z. Zou, *Adv. Funct. Mater.*, 2015, **25**, 998–1013.
19 H. Li, W. Tu, Y. Zhou and Z. Zou, *Adv. Sci.*, 2016, **3**, 1500389–1500391.
20 Z. F. Jiang, W. M. Wan, H. M. Li, S. Q. Yuan, H. J. Zhao and P. K. Wong, *Adv. Mater.*, 2018, **30**, 1706108–1706117.
21 X. She, J. Wu, H. Xu, J. Zhong, Y. Wang, Y. Song, K. Nie, Y. Liu, Y. Yang, M.-T. F. Rodrigues, R. Vajtai, J. Lou, D. Du, H. Li and P. M. Ajayan, *Adv. Energy Mater.*, 2017, **7**, 1700025–1700032.
22 J. Wang, X. Zuo, W. Cai, J. Sun, X. Ge and H. Zhao, *Dalton Trans.*, 2018, **47**, 15382–15390.

23 N. S. Platakis and H. C. Gatos, *Phys. Status Solidi A*, 1972, **13**, K1–K4.
24 J. Black, E. M. Conwell, L. Sigle and C. W. Spencer, *J. Phys. Chem. Solids*, 1957, **2**, 240–251.
25 J. Tan, W. Yang, Y. Oh, H. Lee, J. Park and J. Moon, *ACS Appl. Mater. Interfaces*, 2018, **10**, 10898–10908.
26 L. Zhang, Y. Li, C. Li, Q. Chen, Z. Zhen, X. Jiang, M. Zhong, F. Zhang and H. Zhu, *ACS Nano*, 2017, **11**, 12753–12763.
27 A. Liao, H. He, Z. Fan, G. Xu, L. Li, J. Chen, Q. Han, X. Chen, Y. Zhou and Z. Zou, *J. Catal.*, 2017, **352**, 113–119.
28 L. Bi, X. Gao, L. Zhang, D. Wang, X. Zou and T. Xie, *ChemSusChem*, 2018, **11**, 276–284.
29 S. Li, L. Hou, L. Zhang, L. Chen, Y. Lin, D. Wang and T. Xie, *J. Mater. Chem. A*, 2015, **3**, 17820–17826.
30 Y. Zhou, M. Leng, Z. Xia, J. Zhong, H. Song, X. Liu, B. Yang, J. Zhang, J. Chen, K. Zhou, J. Han, Y. Cheng and J. Tang, *Adv. Electron. Mater.*, 2014, **4**, 1301846–1301854.
31 S. Lu, Y. Zhao, C. Chen, Y. Zhou, D. Li, K. Li, W. Chen, X. Wen, C. Wang, R. Kondrotas, N. Lowe and J. Tang, *Adv. Electron. Mater.*, 2018, **4**, 1700329–1700337.
32 A. Z. Liao, H. C. He, L. Q. Tang, Y. C. Li, J. Zhang, J. N. Chen, L. Chen, C. F. Zhang, Y. Zhou and Z. G. Zou, *ACS Appl. Mater. Interfaces*, 2018, **10**, 10141–10146.
33 J. J. Deng, X. X. Lv, J. Gao, A. W. Pu, M. Li, X. H. Sun and J. Zhong, *Energy Environ. Sci.*, 2013, **6**, 1965–1970.
34 Y. C. Ling, G. M. Wang, H. Y. Wang, Y. Yang and Y. Li, *ChemSusChem*, 2014, **7**, 848–853.
35 H. G. Cha, T. W. Kim and Y. S. Kang, *Mater. Lett.*, 2014, **136**, 245–250.
36 Q. Bu, S. Li, Q. Wu, L. Bi, Y. Lin, D. Wang, X. Zou and T. Xie, *ChemSusChem*, 2018, **11**, 1–10.
37 K. E. Knowles, M. D. Koch and J. L. Shelton, *J. Phys. Chem. C*, 2018, **6**, 11853–11867.
38 B. Liu, Y. Sun, X. Wang, L. Zhang, D. Wang, Z. Fu and T. Xie, *J. Mater. Chem. A*, 2015, **3**, 4445–4452.
39 M. Forster, R. J. Potter, Y. Ling, Y. Yang, D. R. Klug, Y. Li and A. J. Cowan, *Chem. Sci.*, 2015, **6**, 4009–4016.
40 M. Barroso, S. R. Pendlebury, A. J. Cowan and J. R. Durrant, *Chem. Sci.*, 2013, **4**, 2724–2734.